Small heat shock protein HSPB8 interacts with a pre-fibrillar TDP43 low complexity domain species to delay fibril formation

Khaled M. Jami[1], Daniel C. Farb[1], Kayla M. Osumi[1], Catelynn C. Shafer[1], Sophie Criscione[1], and Dylan T. Murray[2*]

[1]Department of Chemistry, University of California, Davis, California, United States of America

[2]Department of Molecular and Cell Biology, University of Connecticut, Storrs, Connecticut, United States of America

*Correspondence: Dylan T. Murray

Email: dylan.murray@uconn.edu

Author Contributions: K.M.J., D.C.F., K.M.O., C.C.S, and S.C., performed the experiments. D.T.M. acquired funding for the research and supervised the experiments. K.M.J. and D.T.M. analyzed data, wrote the manuscript, and conceptualized the experiments.

Competing Interest Statement: The authors declare no competing interests.

Keywords: protein aggregation, liquid droplet, small heat shock protein, protein fibril, RNA-binding protein, biomolecular condensate, ATP-independent chaperone

Abstract

The loss of cellular proteostasis through aberrant stress granule formation is implicated in neurodegenerative diseases. Stress granules are formed by biomolecular condensation involving protein-protein and protein-RNA interactions. These assemblies are protective, but can rigidify, leading to amyloid-like fibril formation, a hallmark of the disease pathology. Key proteins dictating stress granule formation and disassembly, such as TDP43, contain low-complexity (LC) domains that drive fibril formation. HSPB8, a small heat shock protein, plays a critical role modulating stress granule fluidity, preventing aggregation and promoting degradation of misfolded proteins. We examined the interaction between HSPB8 and the TDP43 LC using thioflavin T (ThT) and fluorescence polarization (FP) aggregation assays, fluorescence microscopy and photobleaching experiments, and crosslinking mass spectrometry (XL-MS). Our results indicate that HSPB8 delays TDP43 LC aggregation through domain-specific interactions with fibril nucleating species, without affecting fibril elongation rates. These findings provide mechanistic insight into how ATP-independent chaperones mediate LC domain aggregation and provide a basis for investigating how the TDP43 LC subverts chaperone activity in neurodegenerative disease.

Significance Statement

ATP-independent chaperones facilitate clearance of aggregated proteins through autophagy. This study provides insight into the molecular mechanism by which small heat shock proteins interact with the aggregation-prone low complexity protein domains of RNA-binding proteins linked to neurodegenerative disease pathologies. The results provide a foundation for designing improved chaperones as therapeutics and illustrate a methodology to identify regions in low complexity domains for targeted drug development in the context of neurodegenerative disease.

Main Text

Introduction

A mechanistic understanding of how cells lose the ability to regulate stress granule formation could provide new treatment modalities for neurodegenerative diseases such as amyotrophic lateral sclerosis (ALS), frontotemporal dementia (FTD), and Alzheimer's Disease (AD). Stress granules are cytoplasmic membraneless organelles formed by transient multivalent interactions between proteins, and between proteins and RNA (1). These organelles are thought to be cytoprotective, arresting translational machinery in response to various cellular stresses such as heat shock (2), viral infection (3), and oxidative stress (4).

Many of the proteins driving stress granule and other biomolecular condensation processes have similar functional and structural motifs, often containing RNA-binding domains and an intrinsically disordered low-complexity (LC) domain (5, 6). The defining feature of a LC domain is an amino acid composition biased toward a subset of the 20 naturally occurring amino acids. These LC regions drive biomolecular condensation through transient protein-protein interactions (PPI), especially self-association (7), forming stress granules with fluid liquid droplet properties, (8, 9) and structurally rigid aggregates and amyloid fibrils (10). The molecules in stress granules exhibit highly fluid properties and the formation of the stress granules is reversible. Under prolonged stress, however, the constituent proteins can lose fluidity and form more rigid assemblies. The rigidification process necessarily sequesters and concentrates aggregation-prone LC proteins and increases the likelihood of forming amyloid-like fibrils or other proteinaceous aggregates (11).

Indeed, this molecular aging process is a putative mechanism by which the aggregated foci observed in neurodegenerative disease form (11).

Amyloid-like fibrils and aggregates composed of full-length TDP43 and C-terminal truncations including the LC domain (6, 12, 13) have been found in an increasing number of neurodegenerative diseases, including ALS (14), FTD (15), and the recently classified limbic-predominant age-related TDP43 encephalopathy (LATE) (16). TDP43 is an RNA and DNA binding protein with activities in translation, transcription, and splicing (17). Along with many RNA-binding proteins (RBPs), TDP43 is a major constituent and regulator of stress granules (18–20). Previous work has demonstrated that in vitro liquid droplets have properties akin to cellular stress granules (21–23). In addition, aged liquid droplets consisting of TDP43 LC (24) and TIA1 LC (25) domains form amyloid-like fibrils, further emphasizing the possible link between stress granule aging and pathogenesis.

Crucially, evidence is growing that stress granules are regulated by ATP-dependent molecular chaperones like HSP70 (26), HSP90 (27), and their counterparts the ATP-independent small heat shock proteins (sHSP). sHSP have been found localized within stress granules (28), stabilizing the proteins within (29), and disassembling and degrading aberrant SGs (30, 31). Furthermore, sHSP harbor mutations linked to inherited neuropathies, such as Charcot-Marie-Tooth (CMT) disease and distal hereditary motor neuropathy (dHMN) (32, 33).

HSPB8 is an sHSP that engages in various activities during detrimental proteosome inhibition (34). It is an important component of the protein quality control system where it prevents irreversible aggregation, promotes refolding through its holdase activity, and assists in the degradation of misfolded proteins through recruitment of co-chaperones (26, 35). Additionally, in vivo studies on primary motor neurons (36) and a *Drosophila melanogaste*r model of ALS (37) show that HSPB8 promotes clearance of aggregated TDP43 and reduces TDP43 induced toxicity.

Despite their importance, a complete mechanistic description of how sHSP prevent aggregation and regulate stress granule formation and fluidity does not exist. In this work, we dissect the PPI between the TDP43 LC domain and HSPB8 through thioflavin T (ThT) and fluorescence polarization (FP) aggregation assays, fluorescence microscopy and photobleaching experiments, and chemical crosslinking paired with mass spectrometry (XL-MS). ThT and FP assays report on aggregation and binding kinetics and points to a possible mechanism of inhibition. Fluorescence microscopy experiments monitor changes in TDP43 LC liquid droplet fluidity in the presence of HSPB8. Finally, XL-MS details a putative site of binding between HSPB8 and TDP43 LC. These findings offer insights into the mechanism by which sHSP mitigate protein aggregation, directing future efforts to determine how aggregation-prone RNA-binding proteins like TDP43 evade chaperone activity in neurodegenerative diseases.

Results

To investigate how the chaperone, HSPB8, modulates the assembly kinetics of the TDP43 LC, we first employed a ThT-fluorescence aggregation assay. ThT assays are ideal for detecting amyloid-like protein fibrils and studying their formation kinetics. The use of ThT to monitor TDP43 LC aggregation behavior is well-characterized (24, 38), providing a robust baseline for kinetic perturbation studies.

Fig. 1*A* and *SI Appendix*, Fig. S1 show a pronounced HSPB8 concentration-dependent change in the aggregation behavior of TDP43 LC measured by ThT fluorescence. TDP43 LC aggregation curves were modeled using the approach described by Malmos et al. (39) to extract the apparent rate constant of fibril elongation (k_{app}) and the lag time required to accumulate a critical concentration of fibril-forming nuclei (t_{lag}).

Fig. 1B shows that under the physiological ionic strength and pH conditions used in the aggregation assay, increasing HSPB8 concentrations did not significantly affect k_{app}. However, Fig. 1C shows the dependence of t_{lag} on HSPB8 concentration is consistent with a hyperbolic curve, expected for saturation binding phenomena. Nonlinear regression analysis using a modified Hill Equation provided a measure of the ability of HSPB8 to delay the onset of TDP43 LC aggregation, with a half maximal inhibitory concentration (IC_{50}) of 0.84 ± 0.36 μM. Note here the maximal inhibition is the maximum t_{lag} time for a given TDP43 LC concentration at a set ionic strength and pH. This IC_{50} value indicates moderate affinity between HSPB8 and a species of TDP43 LC present during the aggregation process. This value aligns with previously measured dissociation constants for other sHSP, which are on the order of a few μM for HSPB5 interacting with alpha-synuclein and the beta-amyloid peptide (40–42). The Hill coefficient of 1.4 ± 0.2 suggests no or minimal cooperativity within experimental uncertainty.

HSPB8-dependent lengthening of t_{lag} with no effect on k_{app} suggests that HSPB8 delays TDP43 LC aggregation by interacting with fibril competent nuclei or unfolded soluble proteins, rather than with fibrils or another species contributing to ThT fluorescence. Once nucleation occurs, fibril propagation continues unaffected by HSPB8. Fig. 1D shows that non-specific PPI or crowding were not the cause of the observed effect, as the addition of bovine serum albumin (BSA) as a decoy protein produced no impact on the ThT profile for the TDP43 LC under aggregating conditions.

We hypothesized that the HSPB8 substrate might be a species appearing early in the TDP43 aggregation process, such as soluble or pre-aggregated, nucleation-prone protein. Binding was qualitatively assessed by matrix-assisted laser desorption/ionization mass spectrometry with a time-of-fight mass analyzer (MALDI-TOF). SI Appendix, Fig. S2 shows several low intensity peaks unique to the HSPB8-TDP43 LC mixture consistent with 1^+, 2^+, and 3^+ charged states for a 1:1 complex of HSPB8 and TDP43 LC, suggesting a possible weak PPI between soluble TDP43 LC and HSPB8.

To quantify and directly assess the interaction between HSPB8 and TDP43 LC, we then measured the fluorescence polarization (FP) of fixed amounts of fluorescently labeled HSPB8 with a range of soluble TDP43 LC concentrations. Fig. 2A shows that immediately after mixing (i.e. t = 0), there was a minimal change in FP with increasing concentrations of TDP43 LC. This observation is inconsistent with the MALDI-TOF measurements showing a complex of soluble TDP43 LC and HSPB8. However, the net charge on HSPB8 and TDP43 LC are predicted to be opposite based on calculated isoelectric points (HSPB8, pI = 5.5; TDP43 LC, pI = 10.6). Aberrant gas-phase ion-pairing of HSPB8 and TDP43 LC is thus possible under our pH 7.2 MALDI-TOF measurement conditions. The observation is also inconsistent with HSPB8 binding to natively unfolded TDP43 LC in solution, as a concentration dependent effect would be observed at t = 0 for such a case. The initial FP measurements therefore suggest that the primary substrate of HSPB8 must form as TDP43 LC aggregation progresses.

To probe transient processes in the TDP43 LC aggregation process, such as the formation of fibril-forming nuclei, the FP-based aggregation assay using fluorescein-labeled HSPB8 was monitored over time. Extensive characterization during the optimization of TDP43 LC sample preparation indicates that with agitation, the TDP43 LC aggregation parameters (t_{lag} and k_{app}) are concentration-independent (data provided for review but to be published separately). Therefore, FP results can be compared across varying TDP43 LC concentrations. While Fig. 2A shows little change in HSPB8 FP as a function of TDP43 LC concentration at initial time points, the FP response is consistent with a sigmoidal binding curve after 40 min.

Fig. 2B shows a similar experiment with yeast alcohol dehydrogenase (yADH). The FP values did not plateau within the experimental concentration range, indicating that the binding of HSPB8 to yADH aggregating species is much weaker. Although yADH aggregation produced a larger change in overall HSPB8 FP, the significantly larger mass of yADH, existing as a tetramer of roughly 150 kDa (43), compared to 15.5 kDa TDP43 LC monomers, dictates the polarization response should be larger for HSPB8 binding to yADH than TDP43 LC. These results are intriguing given yADH's common use as a benchmark protein for studying chaperone activity, including HSPB8 (44–46). Nevertheless, SI Appendix Fig. S3 shows our preparations of HSPB8 exhibit the expected chaperone activity on yADH aggregation triggered by a reducing agent.

Throughout the FP aggregation assay, binding isotherms exhibit dynamic behavior, leading to variation in the best-fit parameters to binding models and making singular curve fitting problematic. Instead, the best-fit parameters for a sigmoidal binding model are determined at each time point. These parameter values are then fit to time-dependent functions to obtain a better, global, measurement of the HSPB8-TDP43 LC affinity represented by the complete FP-aggregation assay. Fig. 2C shows the time dependence of these parameters along with the best-fit curves. The complete details are described in the *Materials and Methods* section.

In Fig. 2C, the background fluorescence (FP_{bg}) curve begins high and gradually decays as the b_{max} curve, a measure of the number of available binding sites (e.g. TDP43 LC species capable of binding to HSPB8), increases. Although HSPB8 can form a variety of heterooligomers (47, 48), it is known to exist as a mixture of primarily monomer and homodimer (44–46). The decrease in FP_{bg} is consistent with the presence of a small amount of HSPB8 homodimer that dissociates and contributes to a pool of monomeric HSPB8 that preferentially binds misfolded or fibril-nucleating species of TDP43 LC. Based on the curve fit to FP_{bg}, the background fluorescence equilibrates at 94 min. Data from 94 min and later were thus used to calculate an average K_D of 0.41 ± 0.25 μM, which did not require time-dependent fitting, consistent with a steady-state interaction between HSPB8 and TDP43 LC. Fig. 2D shows the FP binding isotherm calculated from these parameters with the corresponding regions of uncertainty. Table 1 summarizes the fitting parameters obtained from the FP and ThT analyses.

The FP and ThT data together provide more insight into the TDP43 LC aggregation process. The b_{max} curve and ThT data from a concurrently performed ThT aggregation assay with identical starting material were normalized and plotted together in Fig. 2E. An initial increase in FP without significant ThT signal is consistent with HSPB8 interacting with pre-fibrillar TDP43 LC species, likely fibril-competent nuclei, until some critical concentration of these nuclei is reached at t_{lag} (t = 45 min), after which fibril formation and elongation occur, with ThT and FP fluorescence both increasing until the maximal nuclei concentration, the FP or b_{max} maximum, is reached at ~238 min. Then, fibrils become the dominant species; ThT fluorescence plateaus due to saturated binding sites on the fibrils and b_{max} trends downwards as the remaining TDP43 LC molecules are slowly converted to fibrils at the expense of nuclei bound to HSPB8.

To provide a visual characterization of the TDP43 LC during the aggregation process, negative stain TEM images were recorded at various timepoints along the aggregation curve. The images in SI Appendix, Fig. 4 show that initially the TDP43 LC samples are devoid of regularly shaped proteinaceous aggregates, oligomeric assemblies, and fibrils. Short fibrils then form in conjunction with an increase in ThT fluorescence. Elongated, bundled, fibrils are observed in the images once the ThT fluorescence plateau is reached. Across all time points, we did not observe any well-defined assemblies attributable to HSPB8-TDP43 LC complexes or TDP43 LC nuclei. If present, these assemblies were too small for the resolution

of the TEM experiment. Small, white, puncta are observed in some of the images, but they are not regularly shaped or visually identical across the images.

Previous work has shown that HSPB8 plays a role in regulating liquid droplets (30) and stress granules (26). We explored the interaction of HSPB8 with TDP43 LC liquid droplets with fluorescence recovery after photobleaching (FRAP) experiments. SI Appendix Fig. S5 shows a diagram of the sample setup for the confocal microscopy experiments. SI Appendix Fig. S5 also shows TDP43 LC liquid droplets are reliably produced by dilution into PEG-8000 with and without HSPB8. The confocal images in Fig. 3B and SI Appendix Fig. S5 show that HSPB8 preferentially localizes to TDP43 LC droplets. The shallow FRAP curves in Fig. 3A and the persistence of a distinct bleached spot in Fig. 3B indicate that HSPB8 and TDP43 LC co-colocalize and have limited mobility. There is, however, a small but significant increase in the maximum fluorescence recovered after 60 s for TDP43 LC relative to HSPB8 (Welch's t-test, $p = 0.016$, 95% confidence). Additionally, based on the $\tau_{1/2}$ recovery parameters shown in Table 2, TDP43 LC fluorescence recovers two times faster than HSPB8 fluorescence in the mixed droplets. Although droplets of TDP43 LC and HSPB8 at the surface of the microscope slide lack fluidity in the FRAP measurements, SI Appendix, Fig. S6 shows droplet fusion in the bulk solution. Unfortunately, the rapidly moving droplets in solution could not be bleached. Conversely, droplets formed by TDP43 LC alone display significant fluidity at the surface of the microscope slide, with the fluorescence signal shown in Fig. 3C recovering completely after only 30 s. Fig. 3C and D show recovery for whole-droplet bleaching, indicating TDP43 molecules exchange between the concentrated and dilute phases. Fitting parameters from all FRAP assays are shown in Table 2. Altogether, the FRAP data are consistent with HSPB8 holdase activity reducing TDP43 LC mobility in liquid droplets.

Previous studies on sHSP have suggested that the α-crystallin domain (ACD), the disordered N-terminal region (NTR), or both might play a role in chaperone activity (49–54). To identify the regions involved in the interaction between TDP43 LC and HSPB8, we used cross-linking mass spectrometry (XL-MS), a technique that has been used previously to assess the region of interaction between FUS and HSPB8 in liquid droplets (30).

HSPB8 and TDP43 LC were studied independently and jointly to optimize, identify, and categorize the crosslinked species by SDS-PAGE. Fig. 4A and 4B show homomeric crosslinking for both TDP43 LC and HSPB8, consistent with the propensity of TDP43 LC to assemble at neutral pH (38) and HSPB8 to form a dimer (45). Interprotein crosslinking with TDP43 LC is especially challenging due to its namesake low complexity amino acid composition. SI Appendix Fig. S7 shows that including both the N- and C-termini and the overhang after purification tag cleavage, TDP43 LC has only three basic and five acidic residues available for crosslinking. Conversely, HSPB8 has 37 basic and acidic residues available for crosslinking with basic residues biased to within the ACD and acidic residues spread across the entire sequence.

Comparison of the SDS-PAGE images in Fig. 4A with 4C and the cubic spline analyses in Fig. 4B with 4D shows that the amine-amine linkers, bis(sulfosuccinimidyl)suberate (BS3) and glutaraldehyde (Glut), were unable to produce a distinct HSPB8-TDP43 LC linkage. On the contrary, the data in Figure 4 show that the acid-amine linker, 1-ethyl-3-(3-dimethylaminopropyl)carbodiimide (EDC) paired with N-hydroxysulfosuccinimide (sNHS) proved to be highly successful in linking a TDP43 LC monomer with an HSPB8 monomer, the only condition tested which produced a novel crosslinked band. The EDC SDS-PAGE gel strip is only stained with Coomassie blue, while BS3 and Glut gels are both double-stained with Coomassie blue and Silver Stain. Silver stain was used to rule out sparsely populated states because the limit of detection (LOD) for Coomassie blue is ~0.1–0.5 ug (55) while silver stain is approximately 400–2,000X more sensitive with an LOD of 0.25 ng (56). Furthermore, BS3 has a linker length of 11.4 Å

increasing the flexibility and likelihood of a crosslink, while EDC is a 0 Å crosslinker, as the final bond formed is spacer-free native-like amide bond, further highlighting the close HSPB8-TDP43 LC contact indicated by the observed EDC cross-linkage.

To obtain sequence-specific interaction sites, the crosslinked proteins were enzymatically digested, and the resultant peptides analyzed by XL-MS. Fig. 4E shows a cartoon summarizing the XL-MS analysis and SI Appendix Tables S1–S4 list the observed crosslinked peptides. The ambiguous linkages cannot be definitively assigned as occurring between two of the same protein or within the same protein without additional samples and analysis. However, 22 of the 26 (or 85%) unique HSPB8-HSPB8 crosslinked sites are unambiguous linkages within the ACD of HSPB8. In addition, the only confirmed dimer linkage for HSPB8 was found on the ACD, suggesting the dimer is formed through the ACD.

The identified hetero-interprotein crosslinks provide evidence for interactions between the NTR (residues 1–73) and ACD of HSPB8 (residues 74–176) with a fibril-forming core of TDP43 LC (residues 365–400), previously identified by Fonda et al. (24). This result substantiates previous work showing that the both the NTR and ACD of HSPB8 may play roles in substrate recognition, binding, and activity (49–54, 57).

Discussion

sHSP are essential molecular chaperones that preserve cellular proteostasis, uniquely capable of recognizing and stabilizing misfolded or aggregating proteins through remarkably low affinity, transient PPIs. Quantifying the dissociation constants of protein chaperones is incredibly challenging due to inherently weak binding affinities of these PPI, a challenge compounded by the short-lived nature of their substrates. These substrates are highly sensitive, prone to a cascade of misfolding, oligomeric aggregation, and subsequent precipitation, making them difficult to capture. In this manuscript, we have demonstrated two methods to measure the affinity of HSPB8 for a suspected fibril nucleating species of the TDP43 LC. Indirect measurements (IC_{50}) were achieved by assessing how HSPB8 alters the aggregation kinetics of TDP43 LC in a ThT aggregation assay (Fig. 1), while direct measurements (K_D) were obtained through time-dependent fluorescence polarization (Fig. 2). Both methods effectively yield dissociation constants (IC_{50} vs K_D) that are also in good agreement (ThT, IC_{50} = 0.84 ± 0.36 μM; FP, K_D = 0.41 ± 0.25 μM). Due to the simple environment of our in vitro assay, rough equivalence of the measured IC_{50} value with a true K_D is expected. In doing so we have also gained insight into the mechanism of interaction, where HSPB8 delays TDP43 aggregation by inhibition of primary nucleation. A similar chaperoning mechanism has been observed for DNAJB6, a member of the HSP40 family (58).

Although many sHSP readily form higher order oligomers (59–62), these forms are thought to act as “storage” until dissociation into dimers or monomers enables chaperone activity (62–64). Our results are consistent with monomeric HSPB8 binding to monomeric TDP43 LC. This conclusion is supported by several observations. First, the lack of cooperativity (Fig. 1; Hill coefficient, 1.4 ± 0.2) in binding indicates TDP43 LC binds only as a monomer. Second both the background FP and overall change in FP is too low to corroborate either a dimer of HSPB8 interacting with a TDP43 LC monomer or a HSPB8 PPI with anything more than a monomer of TDP43 LC (Fig. 2). Finally, the crosslinking SDS-PAGE gels do not show any evidence of dimeric PPI between HSPB8 and TDP43 (Fig. 4). These results, however, do not preclude the existence of a HSPB8 oligomer. On the contrary, while we observe no evidence for high order oligomers, we observed evidence for a small population of dimeric HSPB8 in equilibrium with monomeric HSPB8. This equilibrium is verified by the MALDI-TOF of HSPB8 presenting a low intensity dimer peak (SI Appendix, Fig S8), the transiently high background FP likely arising from a small population of dimeric HSPB8 (Fig. 2C), and the crosslinking gels consistently depicting both a monomer and dimer for HSPB8 (Fig. 4A and 4C). In

addition, based on the high levels of inter-peptide crosslinking within the ACD determined by XL-MS (Fig. 4C and SI Appendix, Tables S1–S4), we suspect that this region is likely involved in HSPB8 self-association. In other sHSP, the ACD is known to play a significant role in lower level oligomerization, such as dimerization (65–67).

Our data also suggest that TDP43 LC nuclei are in equilibrium with fibrils and that these nuclei are the substrate recognized by HSPB8. The change in FP observed here is not drastic enough to indicate binding to fibrils, and even after 16 h, there still exists concentration-dependent FP, thus some amount of fibril forming competent TDP43 LC nuclei must be available for HSPB8 to bind, even after the system has reached equilibrium in the ThT assay reporting on fibril formation. In addition, HSPB8 only increases the t_{lag} and does not alter the rate of fibril elongation, k_{app}, supporting that HSPB8 only interacts with TDP43 LC nuclei. Changes in k_{app} would suggest a change in the fibril elongation process. Finally, TEM analysis showed no clear signs of HSPB8 interference in the eventual formation of fibrils or direct complex with fibrils through PPI (SI Appendix Fig. S4). TDP43 LC nuclei were also invisible to TEM, possibly a result of their existence as monomers.

Existing FRAP literature on liquid droplets formed by LC proteins often show an increase in fluidity and dynamics with the addition of an sHSP or chaperone (30, 68). Our FRAP experiments reveal a contrary case where the presence of HSPB8 reduces the molecular motion in a liquid droplet (Fig. 3). By confining and reducing the mobility of TDP43 LC within the droplets, the cell's degradation pathways may more efficiently recognize and process aggregating or misfolded proteins (36, 69–72). The holdase mechanism of HSPB8 may itself be involved with the sequestering process, not only limiting the diffusion and conformational mobility of the TDP43 LC, but also preventing exchange with the bulk solution. However, in our experiments, FRAP of liquid droplets is inherently limited to immobilized droplets at the microscope slide surface, potentially causing a self-selection bias for the least mobile population of droplets. Droplet fusion events are observed above the microscope slide surface like those shown in SI Appendix, Fig S5, indicating at least some fraction of the TDP43 LC and HSPB8 containing droplets exhibit very fluid-like properties.

Our crosslinking results implicating a HSPB8-TDP43 LC chaperone interaction after residue 367 in TDP43 LC seem to contradict recent structural studies on tissue from ALS patients with type B FTLD-TDP (residues 282–360) (73) and type A FTLD-TDP (residues 272–360) (74). In the context of an earlier study showing a transient helix formed by residues 321–340 facilitating TDP43 LC self-association and liquid droplet formation (75), these ex vivo structural models suggest TDP43 LC fibril formation arises from the conversion of a transient alpha helix into a beta strand involving residues clearly preceding the HSPB8-TDP43 LC interaction site we identified. However, in vitro results contend that both an expanded alpha helical region (residues 311–360) and a second fibril forming region (residues 365–400) form amyloid fibrils (14, 24, 76, 77). Furthermore, the same study showing that TDP43 LC self-association is mediated by interactions between the alpha helix also showed that residues 382–385 in the second fibril-forming core participate in the self-association of TDP43 LC (75).

One interpretation of these combined results is a model in which TDP43 LC nuclei form through misfolding-induced self-association of residues in the second fibril-forming core. Pathological aggregation then proceeds via fibril formation involving residues prior to 360 due to high local concentrations of TDP43 LC. In this light, HSPB8 could limit fibril formation through holdase activity by inhibiting misfolded TDP43 LC self-association via interactions in the second fibril-forming core. The HSPB8-TDP43 LC complex would then be degradation via autophagy. Fig. 5 illustrates the HSPB8-TDP43 LC model described here. Disease-specific mechanisms such as amino acid changes in TDP43 LC promoting fibril formation in the helical

region would not be intercepted by the chaperone system under this model. Mutations disrupting the HSPB8-TDP43 LC interaction in the second fibril-forming core region would also be detrimental.

However, while we can rule out HSPB8 interactions with the extreme N-terminus of TDP43 LC, we note the residues able to crosslink are simply not sufficiently distributed to capture the full extent of the HSPB8-TDP43 LC interaction. It is entirely possible that HSPB8 recognizes both fibril forming regions of TDP43 LC, but an interaction with the alpha helical region (residues 311–360) is unobserved due to a lack of residues able to crosslink in the region.

In conclusion, our study provides valuable insights into the specific interactions and mechanisms by which HSPB8 modulates TDP43 LC aggregation. Understanding these interactions at a molecular level can inform future therapeutic strategies aimed at mitigating protein aggregation in neurodegenerative diseases. In the biological milieu, HSPB8 is known to form complexes with several different sHSP, ATP-dependent chaperones, and other proteins (26, 48, 83–85). Additionally, HSPB8 has several known locations of phosphorylation, which has been shown to alter the activity of HSPB8 and other sHSP (86–88). These factors likely influence HSPB8 chaperone activity in vivo, placing a limitation on the interpretations and extrapolations of these in vitro results. To fully appreciate the broader implications of the interactions observed here in disease pathology, further research is needed to explore the complex interplay between HSPB8 and its substrates through higher resolution structural studies and in cellular contexts.

Materials and Methods

TDP43 LC Growth and Expression

WT TDP43 LC (residues P262–M414) were recombinantly produced using a pHIS-parallel plasmid (89) that includes a TEV-cleavable N-terminal 6xHis-tag. The plasmids were transformed by heat shock into chemically competent BL21(DE3) E. coli cells. All cells were grown in a shaker incubator at 37 °C and 220 revolutions per minute (RPM). Bacterial cultures were grown in Luria Broth media supplemented with 1% (w/v) glucose in the presence of 100 µg/ml ampicillin to an optical density at 600 nm of 0.6–1.0 measured using a 1 cm pathlength cuvette on an Eppendorf Biospec Kinetic before adding isopropyl β-D-thiogalactopyranoside (IPTG) to 0.5 mM to induce protein expression. The cultures were grown for another 3 h before harvesting the cells by centrifugation at 6,000 g for 15 min. The cell pellets were flash frozen in liquid nitrogen and stored at −80 °C until purification.

TDP43 LC IMAC Purification

Immobilized metal affinity chromatography (IMAC) purification of the TDP43 LC was done as reported previously by Fonda et al. (24) In brief, the cell pellet was resuspended in 35 mL of 6.0 M guanidinium chloride (Gu-HCl), 1% v/v Triton X-100, 500 mM sodium chloride, 50 mM 2-amino-2-(hydroxymethyl)propane-1,3-diol hydrochloride (Tris-HCl), pH 7.5 containing 3 pellets of mini EDTA-free Pierce Protease Inhibitor (ThermoFisher Scientific). The resuspended pellet was sonicated at a 12% duty cycle for 20 min at 30% power using a Branson SFX-250 Sonifier with a 1/4 in. microtip. The lysate was centrifuged at 75,600 g for 30 min at 4 °C, and the supernatant decanted, and filtered through a 0.22 µm PES syringe filter (Millipore). IMAC was performed using a Bio-Rad NGC Quest 10 Plus chromatography system and a 5 mL Bio-Scale™ Mini Nuvia™ IMAC column (Bio-Rad). The column was equilibrated with 6.0 M Urea, 500 mM sodium chloride, 20 mM 2-[4-(2-hydroxyethyl)piperazin-1-yl]ethanesulfonic acid (HEPES), pH 7.5 before loading the filtered cell supernatant. The column was then washed with the equilibration buffer containing 20 mM imidazole, and then the protein was eluted isocratically by raising the imidazole concentration to 200 mM. The presence of highly pure TDP43 LC was assessed by non-reducing denaturing SDS-PAGE.

TDP43 LC His-tag Removal

IMAC purified TDP43 LC was diluted to 20 μM with buffer containing 0.5 M Gu-HCl, 1 mM 1,4-bis(sulfanyl)butane-2,3-diol (DTT), 20 mM 2-morpholin-4-ylethanesulfonic acid (MES), pH 6.0. Tobacco Etch Virus protease (TEV, prepared in-house) was then added to a final concentration of 0.2 μM. The cleavage reaction was run at room temperature (~20 °C) under quiescent conditions. After 4 and 24 h the cleavage reaction mixture was recharged with an additional 1 mM DTT and 0.2 μM TEV, giving final concentrations of 3 mM DTT and 0.6 μM TEV. SDS-PAGE and MALDI-TOF were used to confirm that His-tag cleavage. The TEV reaction was mixed with 5 mL of Nuvia IMAC Ni-charged resin (Bio-Rad) in equilibration buffer and gently swirled before incubation for 30 min at 4 °C. His-cleaved TDP43 LC was eluted by pouring the column over a glass Econo-Column (Bio-Rad), collecting the flow through, and washing the resin with 10 column volumes of 6 M Urea, 500 mM sodium chloride, 15 mM Imidazole, and 20 mM Tris-HCl, pH 7.5.

TDP43 LC CEX Purification

Eluent and wash fractions containing His-cleaved TDP43 LC were dialyzed into 6 M Urea, 10 mM 2-[4-(2-sulfopropyl)piperazin-1-yl]propylsulfonic acid (PIPPS), pH 4.0 using Spectra Por 3 regenerated cellulose, 29 mm flat width dialysis tubing. The protein was then syringe filtered (sterile 0.22 μm, PES) and loaded onto an UNO S6 Column (Bio-Rad) equilibrated in CEX buffer using a Bio-Rad NGC Quest 10 Plus Chromatography system. Purified protein was eluted using the same buffer with a 0–0.2 M sodium chloride gradient over 15 column volumes (CV). Elution fractions were assayed by non-reducing SDS-PAGE. Fractions of his-cleaved TDP43 LC with no impurities observed in the SDS-PAGE gel were pooled, aliquoted, flash frozen in liquid nitrogen, and stored at −80 °C.

HSPB8 Growth and Expression

HSPB8 was recombinantly produced using a pQTEV plasmid (AddGene #34710) (90) containing a TEV cleavage site and an N-terminal 6xHis-tag. The plasmid was transformed into chemically competent BL21(DE3) E. coli cells by heat shock. Bacterial cells were cultured, induced, and harvested identically to the method described for TDP43 LC.

HSPB8 IMAC Purification and His-tag Removal

The cell pellet was thawed on ice for 30 minutes, then resuspended in 36 mL of 25 mM Tris-HCl, pH 8.0 500 mM sodium chloride, 0.25 mg/mL lysozyme, and 3 pellets of mini EDTA-free Pierce Protease Inhibitor (ThermoFisher Scientific). The resuspended pellet was placed on ice and sonicated twice using a Branson SFX-250 Sonifier with a 1/4 in. microtip at 30% power, with a 12% duty cycle, for 10 min. The ice was replaced between each sonification. The lysate was centrifuged at 75,600 g at 4 °C for 30 minutes, then the supernatant was decanted and filtered through a 0.22 μm PES syringe filter (Millipore).

IMAC was completed on a Bio-Rad NGC Quest 10 Plus Chromatography system using a 5 mL Bio-Scale™ Mini Nuvia™ IMAC column (Bio-Rad). The column was pre-equilibrated with 25 mM Tris-HCl, pH 8.0, 500 mM sodium chloride, and 5 mM DTT. DTT was added to buffers immediately before use. The supernatant was loaded onto the column and washed with the equilibration buffer containing 20 mM imidazole. HSPB8 was eluted by the same buffer with an imidazole gradient of 20–500 mM. Elution fractions were assessed by SDS-PAGE then fractions without visible impurity bands were combined and diluted to 15 μM HSPB8 with equilibration buffer.

TEV protease (prepared in-house) was added immediately after dilution at a molar ratio of 100:1 (HSPB8:TEV) and transferred to Spectra Por 3 regenerated cellulose, flat width 29 mm, dialysis tubing. The TEV reaction was dialyzed at 4 °C for 18–20 hours against 100 mL of 25 mM Tris-HCl, pH 8.0, 5 mM DTT for every 1 mL of 15 μM HSPB8. The protein was harvested and diluted with an equal volume of 25 mM Tris-HCl, pH 8.0, 500 mM Sodium chloride, 20 mM imidazole then 5 mL of Bio-Rad Nuvia IMAC Ni-charged resin in the same diluent buffer was added to the crude cleavage reaction. The mixture was gently swirled before incubation for 30 min at 4 °C with gentle rotation. His-cleaved HSPB8 was eluted by pouring the mixture over a glass Econo-Column (Bio-Rad), collecting the flow through, and washing the resin with the diluent buffer. Eluent and wash fractions containing HSPB8 were then dialyzed overnight in 25 mM Tris-HCl, pH 8.0, and 5 mM DTT. Protein was placed at 4 °C for short term storage (1 week) or combined with an equal volume of 50% V/V glycerol and kept at −80 °C for long-term storage.

Thioflavin T Aggregation Assays

A stock ThT solution, >500 μM, was prepared by dissolving solid ThT (Acros Organics) in ultrapure water. The stock solution was filtered through a sterile 0.22 μm PES membrane (Millipore). The ThT concentration was determined by absorbance at 412 nm on an Eppendorf BioSpectrometer Kinetic using a molar absorption coefficient, ε_{412}, of 36,000 M^{-1} cm^{-1} and a 1 mm path length cuvette. Working solutions were prepared by diluting the stock solution to 60 μM ThT, 450 mM sodium chloride, and 20 mM Tris-HCl, pH 7.5. All ThT solutions were encased in aluminum foil and stored at 4 °C for up to 7 d.

CEX purified TDP43 LC was removed from the −80 °C and thawed at 4 °C. The TDP43 LC was then concentrated to 600 μM using an Amicon Ultra 0.5 mL 3K MWCO centrifugal filter and centrifugation at 14,000 g in 5–10 min intervals. TDP43 LC was diluted to 60 μM with 20 mM Tris-HCl, pH 7.5 immediately before use. HSPB8 was concentrated to 60 μM into 20 mM Tris-HCl, pH 7.5, 5 mM DTT using Amicon Ultra 0.5 mL 3K MWCO centrifugal filters and centrifugation at 5,000 g in 5–10 min intervals at 4 °C. At each interval in the protein concentration process, the tubes were inverted to ensure the most uniform concentration of the protein possible.

To help reduce temperature edge effects, the outer wells of a black-bottom 96 well plate were filled with 200 μL ultrapure water each, sealed with low autofluorescence Thermo Scientific™ Nunc™ adhesive seals, and preheated to 37 °C. Each sample well was adjacent to at least 2 water wells or 2 sample wells in every direction.

Finally, 300 μL solutions of each condition for the aggregation assay were prepared from stock solutions of 60 μM ThT, 60 μM TDP43, a varying amount of HSPB8, and 20 mM Tris-HCl. The final buffer components are 20 mM Tris-HCl, pH 7.5, 150 mM sodium chloride, 1.7 mM DTT, with 20 μM ThT, 20 μM TDP43 LC, and variable amounts of HSPB8. Each well was then filled with 90 μL of sample, immediately sealed with low autofluorescence Thermo Scientific™ Nunc™ adhesive seals, and placed inside a BioTEK Synergy H1 plate reader. ThT fluorescence measurements were recorded in 5 min intervals for up to 18 h, at 37 ° C, with excitation at 440 nm, emission at 485 nm, and 30 s of linear shaking at the instrument's maximum speed before each read. The bandwidth was 9 mm for both excitation and emission. The instrument gain was fixed at 100 and an optimal read height of 5.75 mm was determined by the instrument software for the 90 μL samples.

Thioflavin T Aggregation Data Analysis

Data analysis was performed as described by Malmos et al. (39) In brief, data were normalized using:

$$y_{norm} = \frac{y - y_{min}}{y_{max} - y_{min}}$$

where y_{norm} is the normalized value, y is the raw fluorescence intensity, y_{min} and y_{max} are the minimum and maximum fluorescence values for a single trial. Using non-linear least squares analysis in Python the normalized data was fit to the following equation:

$$y_{norm} = y_s + m_i t + \frac{y_f + m_f t}{1 + e^{-\left[\frac{t - t_{0.5}}{\tau}\right]}}$$

where t is time. The remaining parameters were obtained from the least squares analysis, where y_s and y_f are the initial and final ThT fluorescence intensities, m_i and m_f are the baseline slopes before and after the rapid rise in fluorescence, $t_{0.5}$ is the time to achieve half of the maximal fluorescence intensity, and τ is the elongation time constant.

The apparent fibril elongation rate, k_{app}, and the lag time to fibril formation, t_{lag}, were obtained from:

$$k_{app} = \frac{1}{\tau}$$

$$t_{lag} = t_{0.5} - 2\tau$$

The final plots after fitting shown in Fig. 1A were normalized for ease of comparison.

Using non-linear least squares analysis in Python the lag time plot as a function of HSPB8 concentration was fit to a modified Hill Equation:

$$t_{lag}(H) = \frac{\mu_{max} \cdot [H]^n}{IC_{50} + [H]^n} + t_{lag,T}$$

where μ_{max} is the maximum achievable lag time, $t_{lag,T}$ is the basal lag time determined from TDP43 LC alone, IC_{50} is the half maximal inhibitory concentration, *[H]* is the concentration of HSPB8, and n is the Hill coefficient, a measure of cooperativity.

yADH Turbidity Assay

Yeast alcohol dehydrogenase (yADH, Sigma Aldrich) was dissolved in 50 mM sodium phosphate, pH 8.0, 100 mM sodium chloride and filtered with a 0.22 µm syringe filter. The concentration was determined by UV-Vis absorbance at 280 nm ($E^{1\%}$ = 14.6). HSPB8 and yADH were combined and incubated for 10 minutes at RT, then diluted with 50 mM sodium phosphate, pH 8.0, 100 mM sodium chloride and 1 M DTT (separately) to achieve final concentrations of 0.2 mg/mL (9 µM monomeric) HSPB8, 12.5 mg/mL (90 µM tetrameric) yADH, and 20 mM DTT. The assay was performed using a BioTEK Synergy H1 plate reader set to 42 °C with 360 nm absorbance readings taken every 30 s for 1 h total. Each condition was performed in triplicate with 150 µL in each well. Curves were fit to the same equation described for the ThT aggregation assays to obtain t_{lag} and k_{app}.

MALDI-TOF

TDP43 LC diluted to 40 μM and buffer exchanged into 20 mM ammonium formate, pH 3.0 using 3K MWCO Amicon Ultra-0.5 mL centrifugal filters with centrifugation at 14,000 g in 10 min intervals. Using the same procedure, HSPB8 was concentrated to 20 μM and buffer exchanged into 20 mM Ammonium Acetate, pH 7.2. For the combined TDP43 LC and HSPB8, they were mixed at a 1:2 molar ratio, in 20 mM Ammonium Acetate, pH 7.2 for 10–15 min before spotting.

Matrix solution was made by combining saturated 2,6-dihydroxyacetophenone in 96% ethanol and 18 mg/mL diammonium citrate in ultrapure water at a 3:1 ratio (v/v). MALDI-TOF samples were prepared by combining 2 μL of protein, 2 μL of 2% trifluoroacetic acid in ultra-pure water, and 2 μL of matrix solution. Finally, 1 μL of each sample was spotted on a 384-target ground steel plate and dried under vacuum for 15 min. All MALDI-TOF measurements were performed on a Bruker UltraFlextreme equipped with a 2 kHz SmartBeam laser. The instrument was calibrated using Protein Standard II (Bruker). The ion source 1 and 2 voltages were set to 20 kV and 18.25 kV, respectively. The lens detector voltage was set to 2.832 kV using a mass range of 10 to 50 kDa. The matrix suppression was done through deflection using a cut-off of 5 kDa. The spots were ionized by 250 shots in raster mode. Raw data was baseline corrected using flexAnalysis software (Bruker) then normalized and smoothed (Savitzky–Golay filter) in Python.

Transmission Electron Microscopy

Samples were imaged using ultrathin carbon films (<3 nm) on 400 mesh lacey carbon copper grids (Ted Pella). The grids were prepared by adding 5 μL of sample and incubating for 2 min, then washing twice with 10 μL of ultrapure water for ∼10 s, and then stained with 5 μL of a 2% (w/v) uranyl acetate solution for 15 s. Between each step, bulk liquid was wicked away using a laboratory tissue prior to adding the next solution. Grids were imaged on a FEI Talos 120C transmission electron microscope operating at 80 keV.

Fluorescent Labeling

Labeling reactions were conducted in 20 mM HEPES, pH 7.5, and 5 mM DTT by buffer exchanging TDP43 LC or HSPB8 using a centrifugal filter. Reactions used 20-fold molar excess of dye (Alexa Fluor 647 for TDP43 LC or NHS-Fluorescein for HSPB8, ThermoFisher Scientific) and 10 μM protein. For TDP43 LC, the labeling buffer also contained 6 M urea. Reactions were run in the dark at 4 °C under quiescent conditions for 18 h.

Reactions were then quenched by addition of 1 M Tris-HCl, pH 7.5 to 20 mM. Alexa Fluor 647-labeled TDP43 LC was diluted with 20 mM MES, pH 6.0, and 3 M Gu-HCl to 1 μM. Fluorescein-labeled HSPB8 was diluted with reaction buffer with 50% glycerol to 1 μM HSPB8 and 25% (v/v) glycerol. Both proteins were aliquoted and stored at −80 °C. Small quantities of the proteins were run on a non-reducing SDS-PAGE gel and imaged on a Bio-Rad ChemiDoc MP gel imager with presets for 647 and 488 nm to confirm labeling.

Before use in fluorescence experiments, fluorescently labeled proteins were thawed at 4 °C and desalted using 7k MWCO, 2 mL Zeba™ Spin Desalting Columns (ThermoFisher Scientific) into 6 M Urea, 10 mM PIPPS, pH 4.0 for TDP43 LC and 5 mM DTT, 20 mM Tris-HCl, pH 7.5 for HSPB8. This was done following the manufacturer's recommendations. For FP experiments, labeled HSPB8 was used neat, for FRAP experiments the labeled proteins were pooled with stock unlabeled protein at a ratio of 1:300 for TDP43 LC and 1:100 for HSPB8 (labeled:unlabeled) and concentrated to 600 μM and 60 μM, following the procedure outlined in Thioflavin T Aggregation Assays.

Fluorescence Polarization

His-cleaved, fluorescein labeled HSPB8 at 5 μM, TDP43 LC at 600 μM, 1 M Tris-HCl, pH 7.5, and ultrapure water were combined to achieve 300 μL of 5 nM HSPB8, 20 mM Tris-HCl, pH 7.5, 150 mM sodium chloride, 2 mM DTT, and various TDP43 LC or yADH concentrations. For triplicate measurements, 90 μL was aliquoted to each well of a black-bottom 96 well plate. Plates were pre-heated to 37 °C and unused outside wells were pre-filled with water following the same procedure described in Thioflavin T Aggregation Assays.

FP assays were performed using a BioTEK Synergy H1 plate reader with parallel and perpendicular filters with excitations at 485 nm and emissions at 528 nm for both. Both sets of filters had 20 nm bandwidths and 510 nm dichroic mirrors. Samples were read from a height of 6 mm every 5 min, for 18 h, at 37 °C, with linear shaking for 30 s at the instrument's maximum speed before each read.

For yADH, lyophilized protein was dissolved in 20 mM Tris HCl, pH 7.5 and mixed with Fluorescein labeled HSPB8 as described above. The samples were incubated at 37 °C for 15 min before the first read and 20.5 h for the second read.

Fluorescence Polarization Data Analysis

The FP response at a given time, *t*, of a mixture of labeled HSPB8 interacting with varying amounts of TDP43 LC that exhibit concentration independent aggregation rates (k_{app}) is expected to take the general form:

$$FP = \frac{b_{max} \cdot [P]}{K'_D + [P]} + FP_{bg}$$

where b_{max} is the apparent fluorescence polarization signal when HSPB8 saturates the available TDP43 LB binding sites (and is related to one or more identical binding sites on a TDP43 LC fibril), *[P]* is the concentration of TDP43 LC, K'_D is the apparent equilibrium dissociation constant for HSPB8 binding to TDP43 LC, and FP_{bg} is the apparent background fluorescence polarization signal. K'_D is used rather than the dissociation constant (K_D) to account for transient HSPB8-TDP43 LC interactions, and both b_{max} and FP_{bg} have time dependence.

FP values as a function of TDP43 LC concentration at each time point were fit to the above model using non-linear least squares analysis in Python. Standard deviations for each parameter were calculated from the diagonal elements of the covariance matrix obtained during the fitting process. Data points were weighted by their uncertainty for curve fitting purposes, using the following relationship:

$$\chi^2 = \sum_{i=0}^{n} \left(\frac{y_i - f(x_i, \mathbf{p})}{\sigma_i} \right)^2$$

where χ^2 is the weighted sum of squared residuals, y_i are the observed values, $f(x_i, \mathbf{p})$ are the predictions using vectorized model parameters, **p**, and σ_i is the sample standard deviation of each data point. The best-fit parameters for b_{max}, K'_D, and FP_{bg} were averaged for each time point to produce the thin lines and error bars in Fig. 2C.

Since these fitting parameters changed over time in the TDP43 LC-HSPB8 experiments, the measured values for these parameters were obtained by fitting the time-dependent averages to separate time-

dependent functions. Final models were chosen based on the lowest Akaike Information Criterion and Bayesian Information Criterion.

For b_{max}, a Monod model with quadratic decay was used:

$$b_{max}(t) = \frac{(B_{max} - bt) \cdot t}{b_{1/2} + t}$$

where, t is time, B_{max} is the maximum fluorescence polarization signal for fully saturated HSPB8-TDP43 LC binding, b is the rate of non-recoverable loss of fluorescence polarization signal, and $b_{1/2}$ is the time required to achieve half of B_{max}.

For FP_{bg}, a sigmoidal model with linear decay was chosen:

$$FP_{bg}(t) = G_{max} - \frac{G_{\Delta} + gt}{1 + e^{-\left(\frac{t}{g_{1/2}}\right)}}$$

where, G_{max} is the maximal background fluorescence polarization signal, g describes the rate of non-recoverable decrease in background FP over time, $g_{1/2}$ is the time to reach half minimal recoverable background fluorescence polarization signal. G_{Δ} is the change in background fluorescence between G_{max} and the equilibrated background fluorescence signal (G_{bg}) of the sigmoidal decrease in fluorescence polarization signal, described by:

$$G_{bg} = G_{max} - G_{\Delta}$$

For K'_D, the final model was a constant value and determined from the average of all data after background intensity reached equilibrium at 94 min. The thick lines in Fig. 2C were obtained from plotting the best fit $b_{max}(t)$ and $FP_{bg}(t)$ equations and the constant K'_D.

The final FP binding curve plotted in Fig. 2D was obtained from:

$$FP = \frac{b_{max} \cdot [P]}{K_D + [P]} + G_{bg}$$

where K_D the average K'_D value after 94 min. To align with conventional reporting of FP binding curves, the background fluorescence, G_{bg}, was excluded for the final plot.

SDS-PAGE Staining and Imaging

Electrophoresis gels were fixed with 50 mL of water for 5 min then fixed and stained for 15 min with a solution containing 0.13% Coomassie Blue, 50% methanol, and 10% acetic acid. Gels were then washed with 100 mL of water and immediately destained twice for 1.5 h each with 25 mL of 12% methanol and 7% acetic acid. Gels were washed once more with 100 mL of water before imaging. Following Coomassie staining, silver staining was performed using a Pierce Silver Stain Kit (ThermoScientific). Washed gels were sensitized with gel sensitizer for 1 minute, washed with 50 mL of water, stained with silver stain for 30

minutes, washed with 50 mL of water, and finally the silver was reduced by developer for 2–3 min. The developer was quenched with 50 mL of 5% acetic acid for 10 min. Gels were washed with 100 mL of water before imaging using identical parameters. Images were taken on an ChemiDoc Imaging System (BioRad), using the white sample tray and Coomassie Blue or Silver Stain presets with auto-exposure.

EDC Crosslinking

Pierce 1-ethyl-3-(3-dimethylaminopropyl)carbodiimide hydrochloride (EDC) No-Weigh™ Format (ThermoFisher Scientific) and sodium;1-hydroxy-2,5-dioxopyrrolidine-3-sulfonate (sNHS, ThermoFisher Scientific) were dissolved in 20 mM MES to make 50 mM stock solutions. Stock solutions of proteins were prepared following the procedure outlined in Thioflavin T Aggregation Assays section. The final concentration for TDP43 LC was 600 μM and 60 μM for HSPB8.

TDP43 LC, EDC, and sNHS stock solutions were combined at a molar ratio of 1:50:100 to achieve final concentrations, 250 μM TDP43 LC, 12.5 mM EDC, and 25 mM sNHS and allowed to react for 15 min. Afterwards, the reaction was quenched with 1 M DTT stock solution to a final DTT concentration of 20 mM. HSPB8 was concentrated to 24 μM in 20 mM MES, pH 6.5, and combined with 1:50:100 EDC and sNHs and allowed to react for 15 min. Then the sNHS-activated HSPB8 was buffer exchanged into 20 mM HEPES, pH 8.0 and 5 mM DTT using 7k MWCO, 2 mL Zeba™ Spin Desalting Columns (ThermoFisher Scientific). The NHS-labeled TDP43 LC was then diluted with 22 μM sNHS-labeled HSPB8 in 20 mM HEPES, pH 8.0 and 5 mM DTT at a ratio of 1:12.5 (v/v) giving final concentrations of 20 μM for both TDP43 LC and HSPB8. Proteins were crosslinked at room temperature, under quiescent conditions for 30 min. The crosslinking reactions were quenched with 1 M Tris-HCl, pH 7.5 stock solution to a final concentration of 20 mM Tris-HCl. Crosslinked proteins were analyzed by SDS-PAGE.

Amine-Reactive Crosslinking

Pierce bis(sulfosuccinimidyl) suberate (BS3) No-Weigh™ Format (ThermoFisher Scientific) was dissolved in 20 mM HEPES pH 7.5 to make a 50 mM stock solution. Glutaraldehyde stock solutions at 2.6 M were diluted to 50 mM in 20 mM HEPES pH 7.5 immediately before use. TDP43 LC and HSPB8 were prepared following the procedure outlined in Thioflavin T Aggregation Assays to starting concentrations of 600 μM and 60 μM, respectively. Protein solutions were diluted to 20 μM with 20 mM HEPES, pH 7.5 at a molar ratio of 1:50 (protein to crosslinker) and allowed to react for 30 min. The reactions were then quenched with 1 M Tris-HCl, pH 7.5 to a final concentration of 20 mM Tris-HCl. Crosslinked proteins were analyzed by SDS-PAGE.

Protein Digestion and Peptide Desalting

Quenched crosslinking reactions were buffer exchanged using 7k MWCO, 2 mL Zeba™ Spin Desalting Columns (ThermoFisher Scientific) into 1 M Gu-HCl, 20 mM Tris-HCl, pH 7.5. Reactions were reduced by the addition of 0.5 M TCEP to 5 mM and heating to 56 °C for 30 min. Acetylation was performed by adding 500 mM iodoacetamide (IAA) to 10 mM and incubating in the dark at RT for 1 h. Acetylation was then quenched for 15 min at RT by the addition of 1 M DTT to 15 mM.

Acetylated proteins were then buffer exchanged using 10K MWCO Amicon Ultra-15 centrifugal filters with centrifugation at 3000 x g in 20 min intervals into 1 M Urea, 20 mM Tris, pH 7. Proteins were digested for 1 h at 37 °C after the addition of 1 mg/mL Trypsin (proteomics grade, Sigma-Aldrich) in 50 mM acetic acid at a 1:100 mass ratio (trypsin:protein). A secondary digestion was performed for 18 h at room temperature by the addition of 0.5 mg/mL chymotrypsin (sequencing grade, Promega) in 1 mM HCl at a 1:100 mass ratio (chymotrypsin:protein). SDS-PAGE was used to confirm complete digestion of the crosslinked proteins.

Digested proteins were desalted and concentrated using C18, 0.6 uL bed volume, 10 µL tip volume ZipTip® Pipette Tips (Millipore Sigma) following the manufacturer's recommendations. Desalted peptides were then lyophilized and resuspended in 0.1% trifluoroacetic acid (TFA).

Mass Spectrometry

Peptides were fractionated over 40 min at 0.500 $\mu l \cdot min^{-1}$ on a PepSep, 150 µm x 25 cm, 1.5 µm particle size, 100 Å pore, C18 analytical column (Bruker), heated to 49 °C, with 6–99% variable gradient (SI Appendix, Fig. S9). One µg of total peptides was injected and analyzed on an Orbitrap Exploris 480 using a MS1 scan range of 350-1500 (m/z), 1 microscan, normalized automatic gain control (AGC) target at 10^6, radio frequency (RF) lens at 45%, in monoisotopic precursor selection (MIPS) mode. The minimum intensity was set to 5000 and charge states were filtered to include only charges 2–6. A dynamic exclusion filter was set to exclude after 1 time, for 30 s, using a mass tolerance of ± 10 ppm. Data dependent MS/MS was used to filter peptides for fragmentation, using 30 scans and a 1.6 m/z isolation window. Peptides were fragmented using a normalized higher-energy collisional dissociation (HCD) energy of 30%, an AGC target of $4 \cdot 10^5$, 1 microscan, 40 ms ion accumulation time, RF lens set to 50%, with the first mass cutoff set to 170 (m/z). Data was set to centroid and MS1 and MS2 resolutions are 60000 and 15000 FWHM at 200 m/z, respectively.

XL-MS Data Processing

Crosslinked peptides were identified using pLink2 (91). Search parameters were 20 ppm precursor mass tolerance, 50 ppm fragment mass tolerance, a minimum of 6 and a maximum of 60 amino acids per chain, and a peptide mass minimum of 600 and maximum of 6000 Da per chain. The crosslinker option was either BS3 or EDC-DE. A fixed modification was added for carbamidomethy (C; 57.02146) and variable modifications were added for deamidation (N, Q; 0.984016), oxidation (M; 15.994915), carbamyl (K, N-terminus 43.005814). Trypsin and chymotrypsin were defined as a single custom enzyme with cleavage at the C-terminal side of FMLWYRK, with cleavage ignored when P1′ is Proline. Filter tolerance was set to ± 10 ppm using a 1% false discovery rate (FDR), separated for each subset of crosslinks (crosslink, looplink, monolink).

Fluorescence Recovery After Photobleaching

Fluorescent protein was prepared as described in *Fluorescence Labeling* section. Liquid droplets consisting of TDP43 LC with 1:300 (labeled:unlabeled) fluorescent protein were formed by diluting 600 µM TDP43 LC in 6 M Urea, 10 mM PIPPS, pH 4.0 30-fold to 20 µM TDP43 LC with a final buffer composition of 10% (w/v) PEG-8000, 150 mM sodium chloride, 20 mM Tris-HCl, pH 7.5. Droplets containing both TDP43 LC and HSPB8 were prepared by diluting 60 µM HSPB8 in 20 mM Tris-HCl, pH 7.5, 5 mM DTT composed of 1:100 (labeled: unlabeled) fluorescent HSPB8 to 20 µM into the same buffer used for TDP43 LC. For each condition, 100 µL was prepared. Droplet formation was confirmed by bright-field microscopy using an Olympus BX51 light microscope with differential interference contrast (DIC) filters, a 40× objective lens, and a Diagnostics Instruments RT Slider camera with 6-megapixel sampling.

The samples were imaged by placing a pre-greased (silicon high-vacuum grease, DOW) PTFE O-ring, 006 Dash Number, ⅛″ ID, and ¼″ OD (Grainer) onto a 24 mm x 50 mm rectangular, #1.5H precision cover glass (ThorLabs). Then, 15 µL of the droplet solution was pipetted into the center of the O-ring and a half coverslip was placed on top. A diagram for sample preparation is in SI Appendix Fig S5.

Recovery After Photobleaching (FRAP) experiments were performed using a Zeiss LSM 980 Aryscan confocal microscope with a Plan-Apochromat 63x/1.4 Oil DIC M27 objective using the Zen software

package. Bleaching on the green and red fluorescence channels used 488-nm and 639-nm laser lines, respectively. Digital gain was set to 1 and offset to was set to 0. For 639 nm only measurements, the laser power was set to 0.8 %. When performing dual laser experiments, the 639 nm channel was set to 1.0% and the 488 nm channel was set to 0.15%. Pre-bleach fluorescence intensity was measured for 4 s, each spot was then bleached 5 times over the course of 0.23 s, and the post-bleach intensity was measured every 1 s for 1 min of recovery time. Raw FRAP data was normalized by setting the pre-bleach intensity to 1 and the post-bleach to 0, averaged (n = 4), then analyzed in Python by least-squares fitting to the following function:

$$I = \theta \cdot (1 - e^{-\beta t})$$

where I is the relative normalized intensity, θ is the fraction of mobile fluorophore which can be used to calculate the immobile fraction (α) by:

$$\alpha = 1 - \theta$$

and β is related to the $\tau_{1/2}$, the time it takes to reach 50% of the mobile fraction intensity (θ), by:

$$\tau_{1/2} = \frac{ln(0.5)}{-\beta}$$

The supplemental bright-field and fluorescence images were captured on an Olympus IX81 inverted microscope equipped with a FV1000 Laser Scanning Confocal Microscope system. Images were taken with a 60x oil immersion objective (Olympus PlanApo N 60x/1.42 na Oil Objective). Fluorescent confocal imaging used an Argon laser with an excitation wavelength of 488 nm at 2.0%, HeNe laser with an excitation wavelength of 633 nm at 10.0%, and an excitation dichroic mirror set to 488/543/633 nm. Fluorescence emission was detected between 510 and 560 nm for the 488 nm line and between 650 and 750 nm for the 633 nm line. Bright field images were recorded on a second channel parallel to the one used to record the fluorescence images. Images were collected using a scan speed of 4.0 μs/pixel, a total area of 640 x 640 pixels.

Acknowledgments

We thank Dr. Steven L. McKnight and Dr. Masato Kato for providing the TDP43 LC plasmid, Dr. William Jewell for assistance with the Mass Spectrometry Core Facility at UC Davis (partially funded by National Institutes of Health Shared Instrumentation award S10OD025271 and S10OD018913), Dr. Bradley Shibata for assistance with the Bio-Electron Microscopy Core Facility at UC Davis, Dr. Gabriela Grigorean for helpful discussions and performing the LC-MS/MS experiments at the Proteomics Core Facility at UC Davis (National Institutes of Health Shared Instrumentation award S10OD026918-01A1), Dr. Thomas Wilkop for assistance with the Light Microscopy Core Facility at UC Davis (partially funded by the National Institutes of Health Shared Instrumentation award 1S10OD026702-01), Dr. Arpad Karsai for assistance with the Keck Spectral Imaging Core Facility at UC Davis, and Dr. Marie Heffern and Dr. Rebeca Fernandez for the use of UV-Vis instrumentation and providing reagents for XL-MS.

Research reported in this publication was supported by the National Institute of General Medical Sciences of the National Institutes of Health under award number R35GM142892 (D.T.M.). The entirety of the research in this publication was supported under this award except for core facility instrument acquisition

and maintenance. The content is solely the responsibility of the authors and does not necessarily represent the official views of the National Institutes of Health.

References

1. T. Hirose, K. Ninomiya, S. Nakagawa, T. Yamazaki, A guide to membraneless organelles and their various roles in gene regulation. *Nat Rev Mol Cell Biol* **24**, 288–304 (2023).

2. F. Palangi, S. M. Samuel, I. R. Thompson, C. R. Triggle, M. M. Emara, Effects of oxidative and thermal stresses on stress granule formation in human induced pluripotent stem cells. *PLOS ONE* **12**, e0182059 (2017).

3. C. McCormick, D. A. Khaperskyy, Translation inhibition and stress granules in the antiviral immune response. *Nat Rev Immunol* **17**, 647–660 (2017).

4. J. R. Wheeler, T. Matheny, S. Jain, R. Abrisch, R. Parker, Distinct stages in stress granule assembly and disassembly. *eLife* **5**, e18413 (2016).

5. T. Arai, *et al.*, TDP-43 is a component of ubiquitin-positive tau-negative inclusions in frontotemporal lobar degeneration and amyotrophic lateral sclerosis. *Biochemical and Biophysical Research Communications* **351**, 602–611 (2006).

6. I. R. Mackenzie, R. Rademakers, M. Neumann, TDP-43 and FUS in amyotrophic lateral sclerosis and frontotemporal dementia. *The Lancet Neurology* **9**, 995–1007 (2010).

7. X. Zhou, *et al.*, Mutations linked to neurological disease enhance self-association of low-complexity protein sequences. *Science* **377**, eabn5582 (2022).

8. E. A. Marnik, D. L. Updike, Membraneless organelles: P granules in Caenorhabditis elegans. *Traffic* **20**, 373–379 (2019).

9. D. S. W. Protter, R. Parker, Principles and Properties of Stress Granules. *Trends in Cell Biology* **26**, 668–679 (2016).

10. A. Molliex, *et al.*, Phase Separation by Low Complexity Domains Promotes Stress Granule Assembly and Drives Pathological Fibrillization. *Cell* **163**, 123–133 (2015).

11. B. Wolozin, P. Ivanov, Stress granules and neurodegeneration. *Nat Rev Neurosci* **20**, 649–666 (2019).

12. B. A. Berning, A. K. Walker, The Pathobiology of TDP-43 C-Terminal Fragments in ALS and FTLD. *Frontiers in Neuroscience* **13** (2019).

13. S. T. Kumar, *et al.*, Seeding the aggregation of TDP-43 requires post-fibrillization proteolytic cleavage. *Nat Neurosci* **26**, 983–996 (2023).

14. Q. Li, W. M. Babinchak, W. K. Surewicz, Cryo-EM structure of amyloid fibrils formed by the entire low complexity domain of TDP-43. *Nat Commun* **12**, 1620 (2021).

15. M. Neumann, *et al.*, Ubiquitinated TDP-43 in Frontotemporal Lobar Degeneration and Amyotrophic Lateral Sclerosis. *Science* **314**, 130–133 (2006).

16. P. T. Nelson, *et al.*, Limbic-predominant age-related TDP-43 encephalopathy (LATE): consensus working group report. *Brain* **142**, 1503–1527 (2019).

17. L. Guo, J. Shorter, Biology and Pathobiology of TDP-43 and Emergent Therapeutic Strategies. *Cold Spring Harb Perspect Med* **7**, a024554 (2017).

18. K. K. McDonald, *et al.*, TAR DNA-binding protein 43 (TDP-43) regulates stress granule dynamics via differential regulation of G3BP and TIA-1. *Human Molecular Genetics* **20**, 1400–1410 (2011).

19. Y. Khalfallah, *et al.*, TDP-43 regulation of stress granule dynamics in neurodegenerative disease-relevant cell types. *Sci Rep* **8**, 7551 (2018).

20. C. Besnard-Guérin, Cytoplasmic localization of amyotrophic lateral sclerosis-related TDP-43 proteins modulates stress granule formation. *European Journal of Neuroscience* **52**, 3995–4008 (2020).

21. A. Patel, *et al.*, A Liquid-to-Solid Phase Transition of the ALS Protein FUS Accelerated by Disease Mutation. *Cell* **162**, 1066–1077 (2015).

22. J. Guillén-Boixet, *et al.*, RNA-Induced Conformational Switching and Clustering of G3BP Drive Stress Granule Assembly by Condensation. *Cell* **181**, 346-361.e17 (2020).

23. D. W. Sanders, *et al.*, Competing Protein-RNA Interaction Networks Control Multiphase Intracellular Organization. *Cell* **181**, 306-324.e28 (2020).

24. B. D. Fonda, K. M. Jami, N. R. Boulos, D. T. Murray, Identification of the Rigid Core for Aged Liquid Droplets of an RNA-Binding Protein Low Complexity Domain. *J. Am. Chem. Soc.* **143**, 6657–6668 (2021).

25. Y. Wittmer, *et al.*, Liquid Droplet Aging and Seeded Fibril Formation of the Cytotoxic Granule Associated RNA Binding Protein TIA1 Low Complexity Domain. *J. Am. Chem. Soc.* **145**, 1580–1592 (2023).

26. M. Ganassi, *et al.*, A Surveillance Function of the HSPB8-BAG3-HSP70 Chaperone Complex Ensures Stress Granule Integrity and Dynamism. *Molecular Cell* **63**, 796–810 (2016).

27. L. Mediani, *et al.*, Hsp90-mediated regulation of DYRK3 couples stress granule disassembly and growth via mTORC1 signaling. *EMBO reports* **22**, e51740 (2021).

28. Z. Liu, *et al.*, Hsp27 chaperones FUS phase separation under the modulation of stress-induced phosphorylation. *Nat Struct Mol Biol* **27**, 363–372 (2020).

29. H. Yu, *et al.*, HSP70 chaperones RNA-free TDP-43 into anisotropic intranuclear liquid spherical shells. *Science* **371**, eabb4309 (2021).

30. E. E. Boczek, *et al.*, HspB8 prevents aberrant phase transitions of FUS by chaperoning its folded RNA-binding domain. *eLife* **10**, e69377 (2021).

31. D. Mateju, *et al.*, An aberrant phase transition of stress granules triggered by misfolded protein and prevented by chaperone function. *The EMBO Journal* **36**, 1669–1687 (2017).

32. O. V. Evgrafov, *et al.*, Mutant small heat-shock protein 27 causes axonal Charcot-Marie-Tooth disease and distal hereditary motor neuropathy. *Nat Genet* **36**, 602–606 (2004).

33. J. Irobi, *et al.*, Hot-spot residue in small heat-shock protein 22 causes distal motor neuropathy. *Nat Genet* **36**, 597–601 (2004).

34. P. Rusmini, *et al.*, The Role of the Heat Shock Protein B8 (HSPB8) in Motoneuron Diseases. *Frontiers in Molecular Neuroscience* **10** (2017).

35. R. M. Hussein, I. J. Benjamin, H. H. Kampinga, Rescue of αB Crystallin (HSPB5) Mutants Associated Protein Aggregation by Co-Expression of HSPB5 Partners. *PLOS ONE* **10**, e0126761 (2015).

36. V. Crippa, *et al.*, The small heat shock protein B8 (HspB8) promotes autophagic removal of misfolded proteins involved in amyotrophic lateral sclerosis (ALS). *Human Molecular Genetics* **19**, 3440–3456 (2010).

37. V. Crippa, *et al.*, The chaperone HSPB8 reduces the accumulation of truncated TDP-43 species in cells and protects against TDP-43-mediated toxicity. *Human Molecular Genetics* **25**, 3908–3924 (2016).

38. W. M. Babinchak, W. K. Surewicz, "Biophysical Studies of LLPS and Aggregation of TDP-43 LCD" in *Protein Aggregation: Methods and Protocols*, Methods in Molecular Biology., A. S. Cieplak, Ed. (Springer US, 2023), pp. 497–513.

39. K. Gade Malmos, *et al.*, ThT 101: a primer on the use of thioflavin T to investigate amyloid formation. *Amyloid* **24**, 1–16 (2017).

40. J. E. Gestwicki, H. Shao, Inhibitors and chemical probes for molecular chaperone networks. *Journal of Biological Chemistry* **294**, 2151–2161 (2019).

41. T. Scheidt, *et al.*, The binding of the small heat-shock protein αB-crystallin to fibrils of α-synuclein is driven by entropic forces. *Proceedings of the National Academy of Sciences* **118**, e2108790118 (2021).

42. P. Karaś, *et al.*, Evolution towards simplicity in bacterial small heat shock protein system. *eLife* **12**, RP89813 (2023).

43. S. B. Raj, S. Ramaswamy, B. V. Plapp, Yeast Alcohol Dehydrogenase Structure and Catalysis. *Biochemistry* **53**, 5791–5803 (2014).

44. M. V. Kim, A. S. Seit-Nebi, S. B. Marston, N. B. Gusev, Some properties of human small heat shock protein Hsp22 (H11 or HspB8). *Biochemical and Biophysical Research Communications* **315**, 796–801 (2004).

45. V. M. Shatov, S. D. Weeks, S. V. Strelkov, N. B. Gusev, The Role of the Arginine in the Conserved N-Terminal Domain RLFDQxFG Motif of Human Small Heat Shock Proteins HspB1, HspB4, HspB5, HspB6, and HspB8. *International Journal of Molecular Sciences* **19**, 2112 (2018).

46. V. M. Shatov, N. N. Sluchanko, N. B. Gusev, Replacement of Arg in the conserved N-terminal RLFDQxFG motif affects physico-chemical properties and chaperone-like activity of human small heat shock protein HspB8 (Hsp22). *PLOS ONE* **16**, e0253432 (2021).

47. A.-P. Arrigo, Human small heat shock proteins: Protein interactomes of homo- and hetero-oligomeric complexes: An update. *FEBS Letters* **587**, 1959–1969 (2013).

48. V. M. Shatov, S. V. Strelkov, N. B. Gusev, The Heterooligomerization of Human Small Heat Shock Proteins Is Controlled by Conserved Motif Located in the N-Terminal Domain. *International Journal of Molecular Sciences* **21**, 4248 (2020).

49. M. L. Plater, D. Goode, M. J. C. Crabbe, Effects of Site-directed Mutations on the Chaperone-like Activity of αB-Crystallin *. *Journal of Biological Chemistry* **271**, 28558–28566 (1996).

50. K. K. Sharma, H. Kaur, K. Kester, Functional Elements in Molecular Chaperone α-Crystallin: Identification of Binding Sites in αB-Crystallin. *Biochemical and Biophysical Research Communications* **239**, 217–222 (1997).

51. ‡ Joy G. Ghosh, § and Marcus R. Estrada, ‡ John I. Clark*, Interactive Domains for Chaperone Activity in the Small Heat Shock Protein, Human αB Crystallin†. *ACS Publications* (2005). Available at: https://pubs.acs.org/doi/full/10.1021/bi0503910 [Accessed 19 July 2024].

52. ‡ Joy G. Ghosh, § and Marcus R. Estrada, ‡ John I. Clark*, Structure-Based Analysis of the β8 Interactive Sequence of Human αB Crystallin†. *ACS Publications* (2006). Available at: https://pubs.acs.org/doi/full/10.1021/bi060970k [Accessed 19 July 2024].

53. N. Jaya, V. Garcia, E. Vierling, Substrate binding site flexibility of the small heat shock protein molecular chaperones. *Proceedings of the National Academy of Sciences* **106**, 15604–15609 (2009).

54. A. Mainz, *et al.*, The chaperone αB-crystallin uses different interfaces to capture an amorphous and an amyloid client. *Nat Struct Mol Biol* **22**, 898–905 (2015).

55. J. L. Brunelle, R. Green, “Chapter Thirteen - Coomassie Blue Staining” in *Methods in Enzymology*, Laboratory Methods in Enzymology: Protein Part C., J. Lorsch, Ed. (Academic Press, 2014), pp. 161–167.

56. Pierce™ Silver Stain Kit. Available at: https://www.thermofisher.com/order/catalog/product/24612 [Accessed 15 July 2024].

57. K. K. Sharma, G. S. Kumar, A. S. Murphy, K. Kester, Identification of 1,1′-Bi(4-anilino)naphthalene-5,5′-disulfonic Acid Binding Sequences in α-Crystallin*. *Journal of Biological Chemistry* **273**, 15474–15478 (1998).

58. C. Månsson, *et al.*, Interaction of the Molecular Chaperone DNAJB6 with Growing Amyloid-beta 42 (Aβ42) Aggregates Leads to Sub-stoichiometric Inhibition of Amyloid Formation *. *Journal of Biological Chemistry* **289**, 31066–31076 (2014).

59. J. Shi, H. A. Koteiche, H. S. Mchaourab, P. L. Stewart, Cryoelectron Microscopy and EPR Analysis of Engineered Symmetric and Polydisperse Hsp16.5 Assemblies Reveals Determinants of Polydispersity and Substrate Binding*. *Journal of Biological Chemistry* **281**, 40420–40428 (2006).

60. G. K. A. Hochberg, J. L. P. Benesch, Dynamical structure of αB-crystallin. *Progress in Biophysics and Molecular Biology* **115**, 11–20 (2014).

61. B. Jovcevski, J. Andrew Aquilina, J. L. P. Benesch, H. Ecroyd, The influence of the N-terminal region proximal to the core domain on the assembly and chaperone activity of αB-crystallin. *Cell Stress and Chaperones* **23**, 827–836 (2018).

62. E. V. Mymrikov, *et al.*, Regulation of small heat-shock proteins by hetero-oligomer formation. *Journal of Biological Chemistry* **295**, 158–169 (2020).

63. E. Åhrman, W. Lambert, J. A. Aquilina, C. V. Robinson, C. S. Emanuelsson, Chemical cross-linking of the chloroplast localized small heat-shock protein, Hsp21, and the model substrate citrate synthase. *Protein Science* **16**, 1464–1478 (2007).

64. D. Cox, E. Selig, M. D. W. Griffin, J. A. Carver, H. Ecroyd, Small Heat-shock Proteins Prevent α-Synuclein Aggregation via Transient Interactions and Their Efficacy Is Affected by the Rate of Aggregation *. *Journal of Biological Chemistry* **291**, 22618–22629 (2016).

65. C. Bagnéris, *et al.*, Crystal Structures of α-Crystallin Domain Dimers of αB-Crystallin and Hsp20. *Journal of Molecular Biology* **392**, 1242–1252 (2009).

66. E. V. Baranova, *et al.*, Three-Dimensional Structure of α-Crystallin Domain Dimers of Human Small Heat Shock Proteins HSPB1 and HSPB6. *Journal of Molecular Biology* **411**, 110–122 (2011).

67. S. Jehle, *et al.*, N-terminal domain of αB-crystallin provides a conformational switch for multimerization and structural heterogeneity. *Proceedings of the National Academy of Sciences* **108**, 6409–6414 (2011).

68. S. Lu, *et al.*, Heat-shock chaperone HSPB1 regulates cytoplasmic TDP-43 phase separation and liquid-to-gel transition. *Nat Cell Biol* **24**, 1378–1393 (2022).

69. D. Kaganovich, R. Kopito, J. Frydman, Misfolded proteins partition between two distinct quality control compartments. *Nature* **454**, 1088–1095 (2008).

70. S. Escusa-Toret, W. I. M. Vonk, J. Frydman, Spatial sequestration of misfolded proteins by a dynamic chaperone pathway enhances cellular fitness during stress. *Nat Cell Biol* **15**, 1231–1243 (2013).

71. R. Cristofani, *et al.*, The Role of HSPB8, a Component of the Chaperone-Assisted Selective Autophagy Machinery, in Cancer. *Cells* **10**, 335 (2021).

72. Y. Li, *et al.*, Hsp70 exhibits a liquid-liquid phase separation ability and chaperones condensed FUS against amyloid aggregation. *iScience* **25**, 104356 (2022).

73. D. Arseni, *et al.*, Structure of pathological TDP-43 filaments from ALS with FTLD. *Nature* **601**, 139–143 (2022).

74. D. Arseni, *et al.*, TDP-43 forms amyloid filaments with a distinct fold in type A FTLD-TDP. *Nature* **620**, 898–903 (2023).

75. A. E. Conicella, G. H. Zerze, J. Mittal, N. L. Fawzi, ALS Mutations Disrupt Phase Separation Mediated by α-Helical Structure in the TDP-43 Low-Complexity C-Terminal Domain. *Structure* **24**, 1537–1549 (2016).

76. Z. Chang, J. Deng, W. Zhao, J. Yang, Amyloid-like aggregation and fibril core determination of TDP-43 C-terminal domain. *Biochemical and Biophysical Research Communications* **532**, 655–661 (2020).

77. X.-F. Zhuo, *et al.*, Solid-State NMR Reveals the Structural Transformation of the TDP-43 Amyloidogenic Region upon Fibrillation. *J. Am. Chem. Soc.* **142**, 3412–3421 (2020).

78. W. Xu, *et al.*, Surface charge and hydrophobicity determine ErbB2 binding to the Hsp90 chaperone complex. *Nat Struct Mol Biol* **12**, 120–126 (2005).

79. E. M. Clerico, J. M. Tilitsky, W. Meng, L. M. Gierasch, How Hsp70 Molecular Machines Interact with Their Substrates to Mediate Diverse Physiological Functions. *J Mol Biol* **427**, 1575–1588 (2015).

80. G. C. Melkani, G. Zardeneta, J. A. Mendoza, Oxidized GroEL can function as a chaperonin. *FBL* **9**, 724–731 (2004).

81. G. B. Reddy, P. A. Kumar, M. S. Kumar, Chaperone-like activity and hydrophobicity of α-crystallin. *IUBMB Life* **58**, 632–641 (2006).

82. R. Singh, Ch. M. Rao, Chaperone-like activity and surface hydrophobicity of 70S ribosome. *FEBS Letters* **527**, 234–238 (2002).

83. S. Carra, S. J. Seguin, H. Lambert, J. Landry, HspB8 Chaperone Activity toward Poly(Q)-containing Proteins Depends on Its Association with Bag3, a Stimulator of Macroautophagy *. *Journal of Biological Chemistry* **283**, 1437–1444 (2008).

84. K. Seidel, *et al.*, The HSPB8-BAG3 chaperone complex is upregulated in astrocytes in the human brain affected by protein aggregation diseases. *Neuropathology and Applied Neurobiology* **38**, 39–53 (2012).

85. A.-P. Arrigo, B. Gibert, Protein interactomes of three stress inducible small heat shock proteins: HspB1, HspB5 and HspB8. *International Journal of Hyperthermia* **29**, 409–422 (2013).

86. A. A. Shemetov, A. S. Seit-Nebi, N. B. Gusev, Phosphorylation of human small heat shock protein HspB8 (Hsp22) by ERK1 protein kinase. *Mol Cell Biochem* **355**, 47–55 (2011).

87. C.-F. Yin, *et al.*, Phosphoproteome Analysis Reveals Dynamic Heat Shock Protein 27 Phosphorylation in Tanshinone IIA-Induced Cell Death. *J. Proteome Res.* **19**, 1620–1634 (2020).

88. M. Mühlhofer, *et al.*, Phosphorylation activates the yeast small heat shock protein Hsp26 by weakening domain contacts in the oligomer ensemble. *Nat Commun* **12**, 6697 (2021).

89. P. Sheffield, S. Garrard, Z. Derewenda, Overcoming Expression and Purification Problems of RhoGDI Using a Family of “Parallel” Expression Vectors. *Protein Expression and Purification* **15**, 34–39 (1999).

90. K. Büssow, *et al.*, Structural genomics of human proteins – target selection and generation of a public catalogue of expression clones. *Microbial Cell Factories* **4**, 21 (2005).

91. Z.-L. Chen, *et al.*, A high-speed search engine pLink 2 with systematic evaluation for proteome-scale identification of cross-linked peptides. *Nat Commun* **10**, 3404 (2019).

92. C. W. Combe, L. Fischer, J. Rappsilber, xiNET: Cross-link Network Maps With Residue Resolution *. *Molecular & Cellular Proteomics* **14**, 1137–1147 (2015).

93. S. Carra, M. Sivilotti, A. T. Chávez Zobel, H. Lambert, J. Landry, HspB8, a small heat shock protein mutated in human neuromuscular disorders, has in vivo chaperone activity in cultured cells. *Human Molecular Genetics* **14**, 1659–1669 (2005).

Figures and Tables

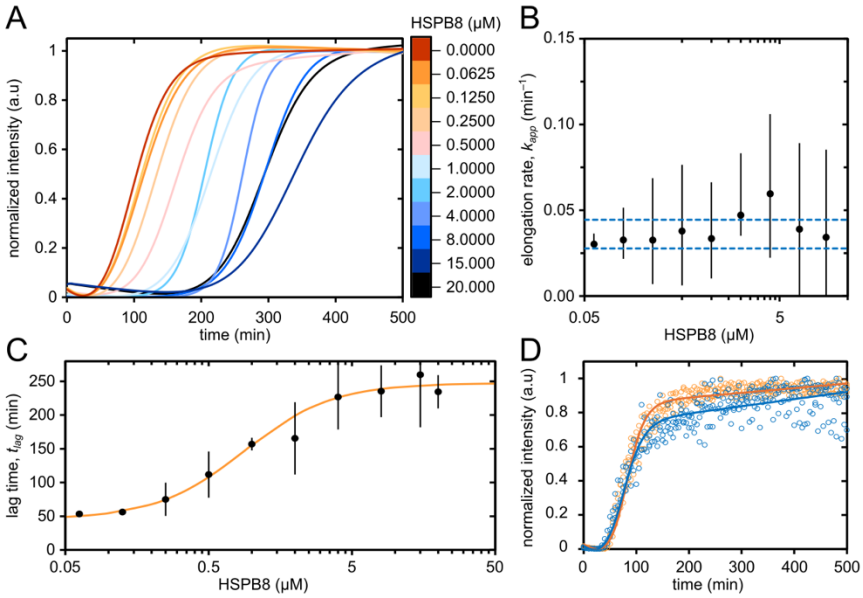

Figure 1. HSPB8 delays aggregation of TDP43 LC by preventing nucleation.
(A) Normalized, best-fit curves to ThT fluorescence data from 20 μM TDP43 LC aggregation assays with varying HSPB8 concentrations. Curves are generated using the average of the best-fit lag time (t_{lag}) and apparent elongation rate (k_{app}) parameters from n = 3 measurements. (B) A plot of the average k_{app} as a function of HSPB8 concentration, p = 0.467 (Kruskal-Wallis test, α = 0.05). Error bars represent the 95% confidence interval. Horizontal dashed blue lines represent the 95% confidence interval for the TDP43 LC only condition (0 μM HSPB8) shown in red in panel (A). (C) A plot of t_{lag} as a function of HSPB8 concentration. A best-fit sigmoidal curve calculated using a modified Hill equation is shown in orange. Error bars correspond to ±1 standard deviation. (D) Normalized ThT fluorescence data and best-fit curves for TDP43 LC aggregation assays with 8 μM BSA (orange) and without (blue). Curves are generated using the average of the best-fit t_{lag} and k_{app} parameters from n = 3 measurements. All experimental measurements are shown as circles in their respective color.

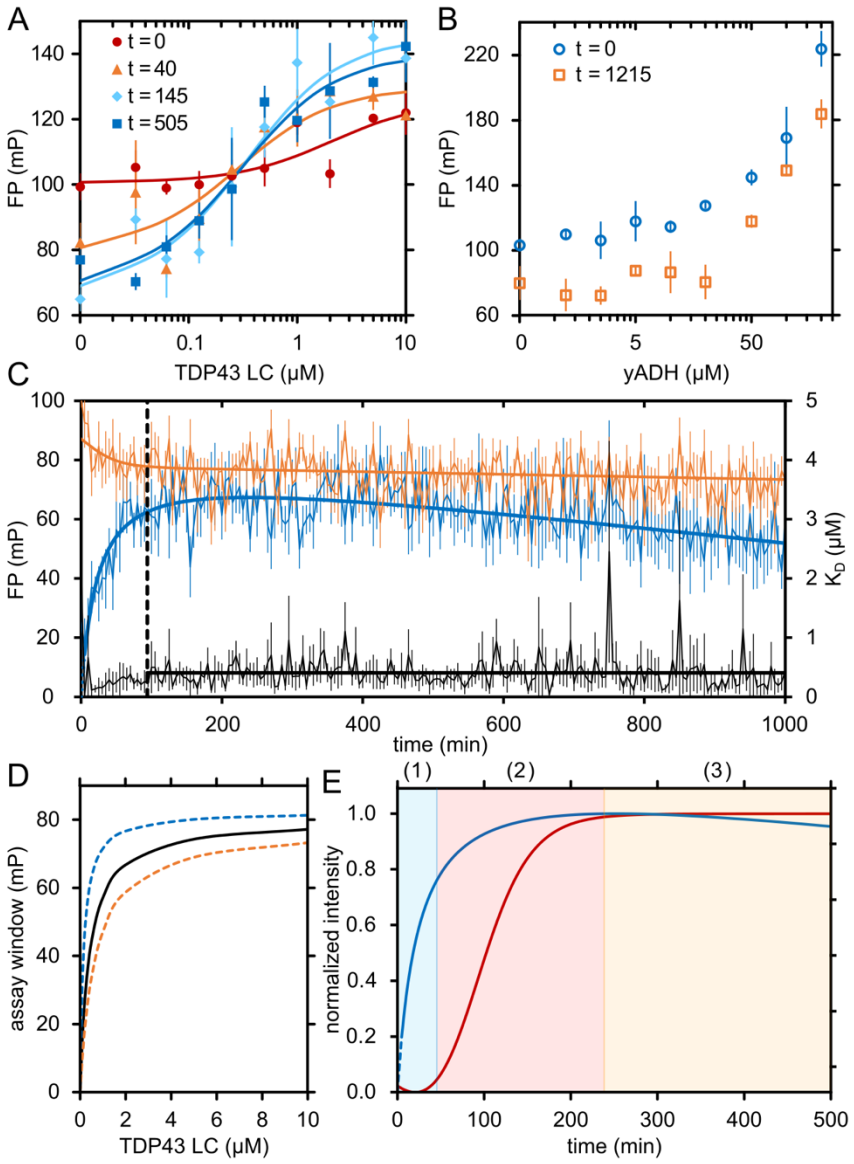

Figure 2. Fluorescence polarization monitors HSPB8 chaperone activity with pre-fibrillar TDP43 LC. (A) Fluorescence polarization (FP) curves at various time points during a TDP43 LC aggregation assay with 5 μM fluorescein-labeled HSPB8. Curves are plotted using the average t_{lag} and k_{app} best-fit parameters from independent fits to data from n = 3 measurements. (B) FP values for the yADH aggregation assay before (t = 0 min) and after temperature induced aggregation (t = 1215 min) with 5 μM fluorescein-labeled HSPB8. For (A) and (B), all points are the average of n = 3 measurements, error bars represent ±1 standard deviation, and legend values are all in minutes. (C) Plot of the best-fit values from the FP aggregation assay. The thin jagged-lines represent the average apparent background fluorescence (FP_{bg}, orange), the average apparent maximum binding capacity (b_{max}, blue), and the average apparent dissociation constant (K'_D, black). The error bars correspond to ± 1 standard deviation from n = 3 measurements. The vertical black dashed line is at 94 min where K_D averaging begins. The thick smooth lines are best-fit curves to the time dependent average of each parameter. (D) A background corrected FP plot generated using the fitted curves from all three separate plots in (C). The blue and orange dashed lines represent the variation in FP

dictated by the standard deviation from the least-squares fit for K_D and B_{max}. (E) Plot of the best-fit curves for the normalized FP b_{max} (blue) and normalized ThT (red) data. The ThT assay was recorded in parallel to the FP assay using 10 μM TDP43 LC, 5 μM HSPB8, and 20 μM ThT. The three highlighted areas correspond to the (1) lag or nucleation phase ending at t_{lag} (45 min), (2) elongation or growth phase ending at the maxima of the b_{max} curve (238 min), and (3) plateau phase.

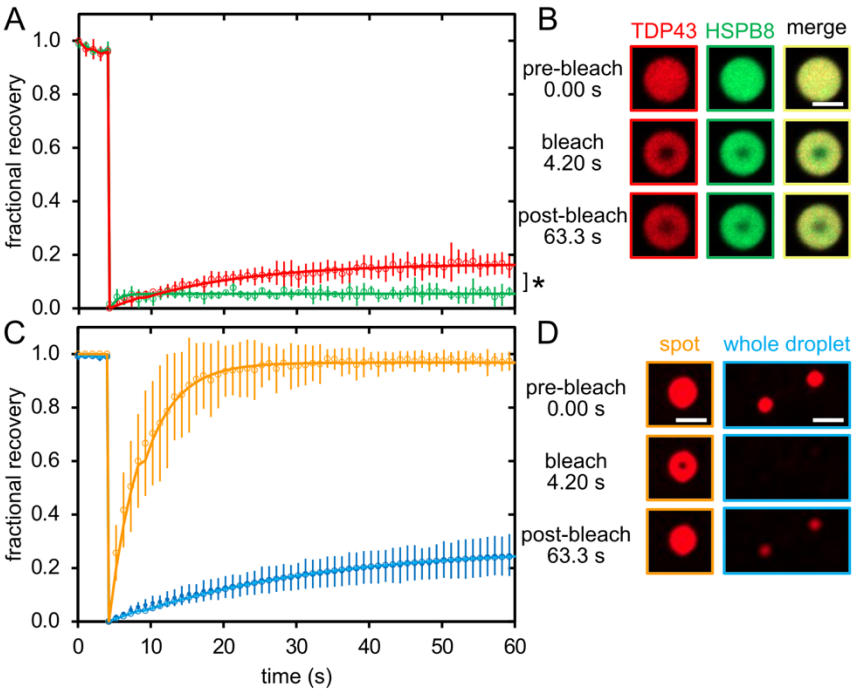

Figure 3. TDP43 LC Liquid droplets are less fluid in the presence of HSPB8.
(A) Fluorescence recovery after photobleaching (FRAP) curves recorded on liquid droplets containing both fluorescein-HSPB8 (Green) and Alexa Fluor 647-TDP43 LC (Red). (B) Confocal images of a representative liquid droplet from the FRAP measurements shown in panel (A). (C) FRAP curves for Alexa Fluor 647-TDP43 LC liquid droplets alone. The orange curve represents a spot based FRAP measurement, the blue curve represents a whole droplet bleaching measurement. (D) Confocal images of representative liquid droplets from the FRAP measurements shown in panel (C). The white inset scale bars are all 2 μM. Each FRAP datapoint is the average of n = 4 measurements and the error bars represent ±1 standard deviation. For bleaching subregions of droplets, the area and laser intensities were the same. Whole droplets were bleached using the entire area of the droplet.

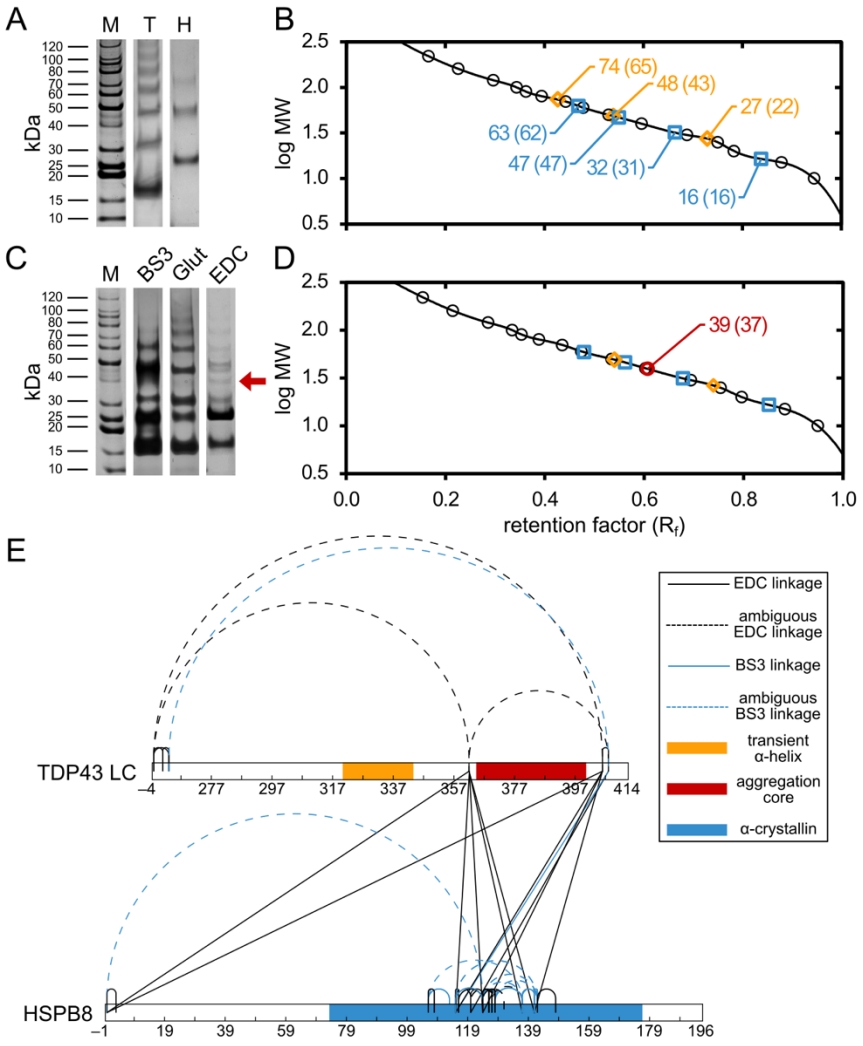

Figure 4. Crosslinking paired with mass spectrometry (XL-MS) identifies a region of interaction between HSPB8 and TDP43 LC.

(A) Strips from an SDS-PAGE gel for the molecular weight marker (M), TDP43 LC only (T), and HSPB8 (H) only. Labels to the left of M correspond to the molecular weights of the marker bands. Both T and H are crosslinked with glutaraldehyde. All gels are stained with Coomassie blue, T was also silver stained. (B) Plot of the best-fit cubic spline function (solid black line) to the molecular weight marker bands (black circles) from the SDS-PAGE gel in (A) used to calibrate migration through the gel to molecular weight. Blue squares correspond to T and orange diamonds correspond to H from panel (A). Only the first 4 bands (monomer, dimer, trimer, and tetramer) are plotted for TDP43 LC and only the first 3 bands are plotted for HSPB8 (monomer, dimer, trimer). Labels indicate the predicted molecular weight from the best-fit cubic spline function, with the value expected from the oligomeric state and primary sequence in parenthesis. (C) Strips from an SDS-PAGE gel for the molecular weight marker (M) and three separate mixtures of TDP43 LC and HSPB8 crosslinked by either BS3, glutaraldehyde (Glut), or EDC. Labels to the left of M correspond to the molecular weights of the marker bands. All gels are stained with Coomassie blue, BS3 and Glut were also silver stained. The red arrow points to the location of a TDP43 LC and HSPB8 heteromeric crosslink. (D) Plot of the best-fit cubic spline function (solid black line) to the molecular weight marker bands (black circles)

in M from (C) used to calibrate migration through the gel to molecular weight. The blue squares and orange diamonds correspond to the identified HSPB8 and TDP43 LC species in panels (A & B) that are also present in the EDC strip from panel (C). The red circle indicates the red arrow in (C) labeled with the molecular weight predicted by the calibration plot next to the expected value for a 1:1 HSPB8-TDP43 LC complex in parenthesis. (E) Crosslink map based on inter- and intrapeptide linkages identified by XL-MS from BS3 and EDC crosslinking. Interpeptide loops are shown as unambiguous, intrapeptide loops are shown as ambiguous, and the domains are defined as transient alpha helix, residues 321–343; aggregation core, residues 365–400; and the alpha crystalin domain (ACD), residues 74–176. The crosslinking map is a modified map generated by xiNET (92).

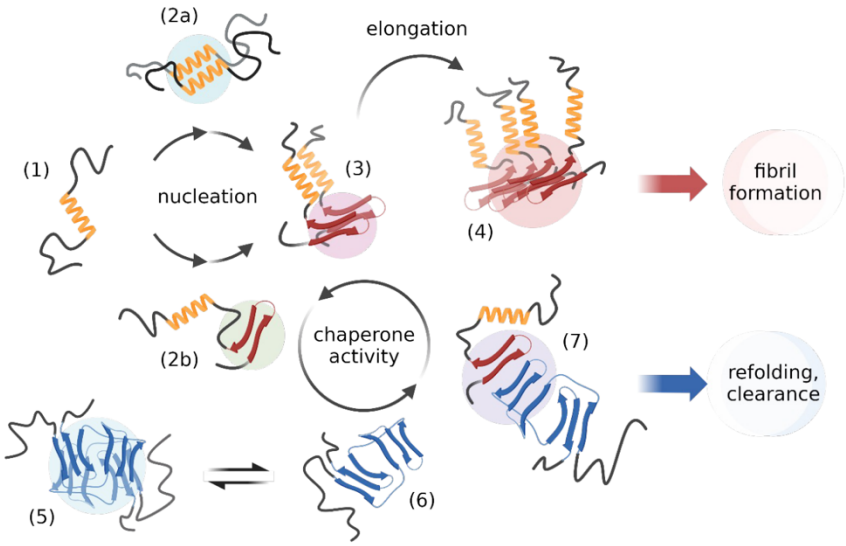

Figure 5. Putative mechanism of aggregation inhibition by HSPB8.
Monomeric TDP43 LC (1) undergoes a nucleation process, oligomerizing (2a) and misfolding (2b) or both. These nuclei (oligomers or misfolded species) promote the misfolding and/or binding of additional misfolded TDP43 LC (3) which then begins the elongation and amyloid fibril formation process (4). Dimeric HSPB8 (5) is in equilibrium with the monomer (6) which disrupts the nucleation process by binding a misfolded nuclei (2b) or possibly dissolving a pre-aggregated species (3). An interaction between the ACD of HSPB8 and the aggregation core of TDP43 LC forms a transient complex (7). Aggregation is delayed through HSPB8 holdase activity until refolding by an ATP-dependent chaperone or clearance by autophagy processes (26, 93). The domain coloring scheme is the same as Fig. 4E with the transient TDP43 LC α-helix in orange, the TDP43 LC aggregation core in red, and the HSPB8 α-crystallin domain in blue.

Table 1: Parameters Derived from ThT and FP Assays.

Component	Description	Assay	Value[a]	Unit
IC_{50}	half maximal inhibitory concentration	ThT	0.84 ± 0.38	μM
K_D	dissociation constant	FP	0.41 ± 0.25	μM
μ_{max}	maximum increase in lag time at saturation	ThT	202 ± 36	min
B_{max}	maximum lossless FP at saturation	FP	80.3 ± 2.3	mP
G_{max}	maximum background FP	FP	96.6 ± 9.6	mP
n	Hill coefficient (cooperativity)	ThT	1.4 ± 0.2	-
t_{lag}	basal lag time	ThT	45.4 ± 0.44	min
$b_{1/2}$	half-time to reach B_{max}	FP	23 ± 3.5	min
$g_{1/2}$	half-time to reach G_{bg}	FP	25 ± 19	min
G_{Δ}	recoverable decrease in background FP	FP	19 ± 9.6	mP
G_{bg}	equilibrated background FP	FP	78 ± 14	mP
g	rate of non-recoverable decay in FP_{bg}	FP	0.0044 ± 0.0019	$mP \cdot min^{-1}$
b	rate of non-recoverable decay in B_{max}	FP	0.027 + 0.03	$mP \cdot min^{-1}$

[a]the uncertainty is the standard deviation from the least squares fit covariance matrix

Table 2: Parameters Derived from the FRAP Assays[a]

Component	HSPB8 (in TDP43 LC droplets)	TDP43 LC (with HSPB8)	TDP43 LC (alone)	TDP43 LC Whole Droplet
immobile fraction (α)	0.9456 ± 0.001	0.8332 ± 0.002	0.0323 ± 0.002	0.7223 ± 0.004
$\tau_{1/2}$	4.98 ± 0.26	14.78 ± 0.46	7.26 ± 0.05	22.46 ± 0.62

[a]the uncertainties are the standard deviation from the least squares fit covariance matrix